INTERNATIONAL JOURNAL FOR NUMERICAL METHODS IN FLUIDS
Int. J. Numer. Meth. Fluids 2011; **00**:1–28
Published online in Wiley InterScience (www.interscience.wiley.com). DOI: 10.1002/fld

A natural neighbour Lagrange-Galerkin method for the simulation of Newtonian and Oldroyd-B free-surface flows

A. Galavís, D. González*and E. Cueto

Aragón Institute of Engineering Research, Universidad de Zaragoza. Zaragoza, Spain

SUMMARY

In this work a method for the numerical simulation of free-surface flows of Newtonian and non-Newtonian flows is developed. The method is based on the employ of three main ingredients. Firstly, an updated Lagrangian approach for the description of the kinematics. This approach is made possible by using natural neighbour Galerkin methods (also known as natural element methods, NEM).This allows the use of the method of characteristics to integrate the equations of motion along the nodal path-lines. The second ingredient relies in the use of a second-order in time method of characteristics, which has proved to be indispensable for an accurate solution of some problems, even very simple ones. Finally, the third ingredient relies on the use of shape constructors (particularly, α-shapes) to avoid the use of boundary markers or, in general, any explicit description of the boundary. After the theoretical description of the proposed method, some examples illustrating its performance are given. Copyright © 2011 John Wiley & Sons, Ltd.

Received ...

KEY WORDS: Meshless; Natural element method; method of characteristics; α-Shapes; Free-surface flows; Non-Newtonian Fluid Mechanics

CONTENTS

*Correspondence to: David González. Edificio Betancourt. Campus Rio Ebro. Universidad de Zaragoza. María de Luna, s.n. E-50018 Zaragoza, Spain. E-mail: gonzal@unizar.es

Contract/grant sponsor: Spanish Ministry of Science and Innovation; contract/grant number: DPI2008-0098

1. INTRODUCTION

Not all fluids present a linear stress-strain rate relationship as could be grasped from Newtonian fluid constitutive equation. Those that do not are collectively named Non-Newtonian, and represent a broad class of very important and interesting fluids both for the academic and industrial worlds. Examples of these fluids can be found almost anywhere, from body fluids as blood or mucus to man-made substances like paint, shampoo or molten plastics. Of course not all non-Newtonian fluids behave in the same manner so many different constitutive equations, with a wide range of complexity, have been developed to describe their mechanical response.

In this work we have but scratched the surface of this broad topic while addressing the matter of simulating viscoelastic fluid flows. The great industrial importance of these fluids has originated a great deal of interest in its numerical simulation from a relatively long time. A great deal of success has been achieved, and nowadays we count with tools to solve a huge deal of non-trivial flows. Abundant literature can be found on the topic. The interested reader can check [38] and [17] as a primer for techniques introduced prior 1983. Still the processes have been plagued with difficulties, many of which seem to come from the so called *high Weissenberg number problem* (the Weissemberg number is a non-dimensional measure of fluid elasticity). Regardless of the employed numerical method or the viscoelastic constitutive equations used, either differential or integral, when the elasticity of the fluid increased by a little measure, the simulation would suffer from a huge loss in accuracy leading to convergence problems. This situation limited the application spectrum of cases, rendering the numerical tools ineffective to deal with industrial grade problems. The initial suspects of this situation were bifurcations in numerical solutions, the possible 3-dimensional effects in 2-dimensional flows and inability to cope with changes in the type of governing equations [15].

At present, the most widely accepted causes for the high We problem are numerical approximation errors. In [38], they are attributed mainly to three sources: First, errors caused by inaccurate integration schemes employed on the coupled non-linear elliptic-hyperbolic equations system governing viscoelastic flows. Second, numerical oscillations caused by trying to solve an ill-posed problem due to the badly chosen approximation spaces for the essential variables. This problem relates to the LBB or inf-sup condition, and has been addressed in [28] and took in account in the solution scheme employed in this work. Lastly, there is the issue of steep boundary layers not being solved in an adequate fashion due to coarse spatial discretisation or a misrepresentation of the domain near singularities. This problem should be mitigated by the meshless character of the method here proposed, as well as the possibility to easily add particles at critical points. Given that our method addresses some of the suspected causes of the high We problem, it would seem plausible to think that we could gain some ground in this field, as an alternative to the upwinding techniques [36] or discontinuous Galerkin methods [34] currently employed to cope with this problem.

In addition to problems inherent to the non-Newtonian character of some fluids here considered, free-surface phenomena always incorporates additional difficulties to the simulation technique at hand. Evolving domains add important difficulties to fixed mesh methods, as those relying on an

DOI: 10.1002/fld

Eulerian approach [35]. Arbitrary Lagrangian-Eulerian (ALE) methods were developed to beat these problems [21] [22]. In ALE methods an artificial velocity is added to the mesh in order to minimize both mesh distortion and the difficulties associated with the free surface. As an alternative, meshless methods are insensitive to mesh distortion, and hence admit the possibility of updated Lagrangian descriptions of the kinematics [27].

In this paper a method based on the natural neighbour Galerkin approach is developed. The choice is not casual, since the members of the family of meshless methods are very numerous. But among these, only a few share some interesting features such as exact imposition of essential boundary conditions and general order of consistency (thus making it suitable for LBB compliance, for instance), among others. Nevertheless, this same formulation could be employed by using, for instance, maximum-entropy approximants [4], MLS methods [7], or any other meshless method satisfying some very basic requirements.

The outline of the paper is as follows. In Section 2 we review the basics of the natural element method, one of the less known meshless methods. In Section 3 the method to detect the boundary on a mehsless method without any connectivity between nodes is explained. It is based on the use of an improved α-shape technique. In Section 4 the governing equations of the problem, firstly for Newtonian fluids, are introduced. Time discretisation deserves a deep study, as will be justified, since standard, first-order algorithms will be shown to fail even for some very simple problems, thus justifying the need for second-order algorithms. This is done in Section 5. Section 6, in turn, deals with the basics of the Oldroyd B constitutive equation for viscoelastic fluids. Although Oldroyd B equations posses well-known limitations, still describe very well some simple non-Newtonian fluids, while presenting the main numerical difficulties associated to the high Weissenberg number. Numerical examples are included in Section 7 that show the potentialities of the proposed method when compared to existing, state-of-the-art techniques. Finally, some conclusions are drawn in Section 8.

2. THE NATURAL ELEMENT METHOD

To explain the appeal of this method to the work here presented, we establish firstly the motivation of this work. Traditionally the fluid models are built using an Eulerian frame of reference [22]. This framework is not particularly well suited for simulating free-surface flows, forcing different authors to tackle the problem with different methods. Several techniques have been developed to keep track of the evolving boundary [23]. Other researchers have decided to change the formulation in order to work with pure or mixed Lagrangian frames of reference [35]. Here an updated Lagrangian fluid model is adopted, which will be described thoroughly in Section 3.

The most prevalent method for solving partial differential equations in a Lagrangian approach is arguably the Finite Element Method. Yet this technique does not cope very well with the high deformation of the mesh which may occur in transient fluid problems, particularly with those featuring free surfaces. In this way seems natural to use a meshless method. One of the main drawbacks of some of these methods is that the unknowns of the discrete system of equations do not correspond with the essential variables of the differential equation (they do not represent nodal velocities, for instance, when solving Navier-Stokes equations). This implies that the imposition of boundary conditions is not straightforward [24]. This can complicate some tasks such as, for instance, fluid-solid kinematic coupling in fluid-structure interaction (FSI) problems.

In general, meshless methods have nice features in some aspects, such as the before mentioned lack of sensitivity to mesh distortion, continuity and level of consistency [7]. But many of them present serious problems when dealing with essential boundary conditions. Only a few of them, namely the natural element method [18] [19] and maximum-entropy approximation [4] [30], are able to overcome this difficulty without loosing other features.

The Natural Element Method (NEM) is a meshless Galerkin procedure based on the natural neighbour interpolation scheme, which in turn relies on the concepts of Voronoi diagrams and Delaunay triangulation to build Galerkin trial and test functions. All of these will be defined and explained in the following sections.

Prepared using fldauth.cls
DOI: 10.1002/fld

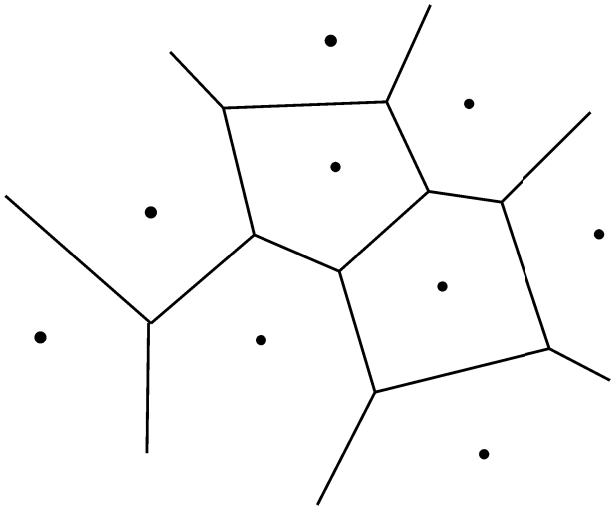

Figure 1. Voronoi Tessellation of a set S of points.

The natural element method allows to bypass the aforementioned problems. First, its meshless character allows us to employ a Lagrangian formulation in situations where large deformation will likely occur, yet the future position of the particles is not known beforehand. We avoid the need for a conscious, and usually very time consuming, mesh generation. Second, by the properties of the method, the inter-domain coupling can be accomplished without any extra difficulty, which also opens the door to also tackle fluid-structure interaction problems.

2.1. Natural neighbour interpolation

With the use of the second-order Voronoi diagram, the relation of neighbourhood of an introduced point with the nearby nodes can be quantified. This is the principle used by Sibson [41], when firstly proposing the natural neighbour interpolation, which is the basis of the NEM. Years later, Belikov [6] introduced a new interpolation scheme, today known as non-Sibsonian (nS) or Laplacian interpolation. More recently, [29] introduced a new class of natural neighbour interpolation constructed over a generalized de Boor algorithm. With this technique, it is possible to generate natural neighbour interpolations with high-order consistency. We briefly review here, for completeness, the basics of natural neighbour interpolation. The interested reader is referred to the original works on the NEM for further details [43] [44] [19] [29].

Given a set of points $S = \ \boldsymbol{x}_0 \ \boldsymbol{x}_1 \ \boldsymbol{x}_2 \qquad \boldsymbol{x}_N \ $, there exists a unique division of the plane such that every region T_i (called Thiessen or Voronoi cell) is closer to a particular point $\boldsymbol{x}_i$ than to any other $\boldsymbol{x}_j$. The union of these areas tessellate the whole plane without gaps or overlapping. This division is called first-order Voronoi diagram [47], and is formally defined as

$$T_i = \ \boldsymbol{x} \qquad ^2 : d(\boldsymbol{x} \ \boldsymbol{x}_i) < d(\boldsymbol{x} \ \boldsymbol{x}_j) \ \ j = i \tag{1}$$

where $d(\ \ )$ denotes the euclidean distance between two points in ^{2}. Figure 1 shows the Voronoi diagram of a set composed of 9 nodes. The cells T_i and T_j are divided by an hyperplane perpendicular to the line that passes through nodes i and j. The intersection between three or more hyperplanes is called Voronoi node or vertex, and is equidistant to all the nodes s_i to which the neighbouring cells T_i are related. The regions can be either closed or unbounded, but always convex.

A higher-order Voronoi tessellation can be defined by including more nodes into the definition. In this manner, a second-order cell T_{ij} is defined as the locus of all the points whose distance to $\boldsymbol{x}_j$ is less than to any other $\boldsymbol{x}_k$ but more than the distance to $\boldsymbol{x}_i$. This can be written as

$$T_{ij} = \ \boldsymbol{x} \qquad ^2 : d(\boldsymbol{x} \ \boldsymbol{x}_i) < d(\boldsymbol{x} \ \boldsymbol{x}_j < d(\boldsymbol{x} \ \boldsymbol{x}_k) \ \ k = j \ \ i \tag{2}$$

Prepared using fldauth.cls
DOI: 10.1002/fld

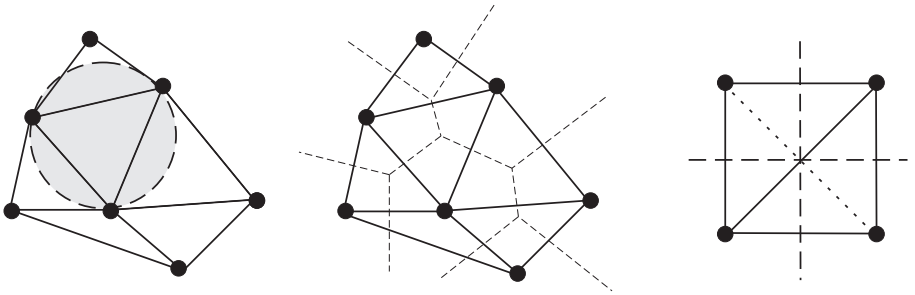

Figure 2. Empty circumcircle. Delaunay triangulation. Degenerated triangulation

This set is non-empty only in the case where T_i borders with T_j. In this case, $\boldsymbol{x}_i$ and $\boldsymbol{x}_j$ are neighbours. The dual structure of the Voronoi tessellation is called Delaunay triangulation [20]. It is constructed by connecting the nodes of S which are neighbours. Of all the possible triangulations, the Delaunay triangles are the ones that maximize the minimal angle. This property make this graph very interesting for mesh generation and as such has been well studied (see [43] and references therein). Figure 2 (b) depicts this triangulation. The Voronoi diagram of this set is shown in dashed lines.

If a circle passing through the three nodes of a triangle $DT(\boldsymbol{x}_i, \boldsymbol{x}_j, \boldsymbol{x}_k)$ (a circumcircle) is drawn, no other node of the set S will be enclosed by it. This property is called the empty circumcircle criterion (Fig 2 (a)). The circumcenter for each triangle is located at the Voronoi vertex where each node's cell converge. There exists a special case on which two (or more) triangles comply with this condition. This occurs when a number of nodes $k \geq d+2$ are located on the same empty n-sphere, where $n = d-1$. In two dimensions this means that at least 4 points are located in the same circle (1-sphere). Thus the Delaunay triangulation may not be unique for a given set of points (Fig 2 (c)).

Let $\boldsymbol{x}$ be a point introduced in the previous set of nodes S. And let $k_i(x)$ and $k(x)$ be the Lebesgue measures of the second order cell $T_{\boldsymbol{xi}}$ and the first order cell $T_{\boldsymbol{x}}$ respectively.

The natural neighbour coordinate of $\boldsymbol{x}$ with respect to node i is defined as the ratio of $k_i(\boldsymbol{x})$ to $k(\boldsymbol{x})$. In two dimensions, the Lebesgue measure k is the area A of the cell.

$$\phi_i(\boldsymbol{x}) = \frac{k_i(\boldsymbol{x})}{k(\boldsymbol{x})} = \frac{A_{T_{\boldsymbol{xi}}}}{A_{T_{\boldsymbol{x}}}} \tag{3}$$

To illustrate the construction of the Sibson interpolant we will present an example. Figure 3 shows a set of 7 nodes to which a point $\boldsymbol{x}$ has been added. The coordinate respect to node 1 of this point is

$$\phi_1(\boldsymbol{x}) = \frac{A_{abfe}}{A_{abcd}} \tag{4}$$

Natural neighbour coordinates can be employed in a Galerkin framework to interpolate the value of some vectorial (or scalar) field $\boldsymbol{u}(x) : \Omega \subset \Re^2 \rightarrow \Re^2$ as

$$\boldsymbol{u}^h(\boldsymbol{x}) = \sum_{i=0}^{N} \phi_i(\boldsymbol{x})\boldsymbol{u}(\boldsymbol{x}_i) = \sum_{i=0}^{n} \phi_i(\boldsymbol{x})\boldsymbol{u}(\boldsymbol{x}_i) \tag{5}$$

where n is the number of natural neighbours of $\boldsymbol{x}$.

Given the interpolant character of the natural neighbour coordinates and some other properties that will be treated next, they have been chosen as the shape functions in a Galerkin method, thus originating the Natural Element Method. Figure 4 depicts the Sibson shape function of a node in a regular grid.

2.2. Natural Element Shape Function Properties

The NEM has interesting qualities which derive from the use of the interpolation functions explained in the previous section. We briefly review them here.

DOI: 10.1002/fld

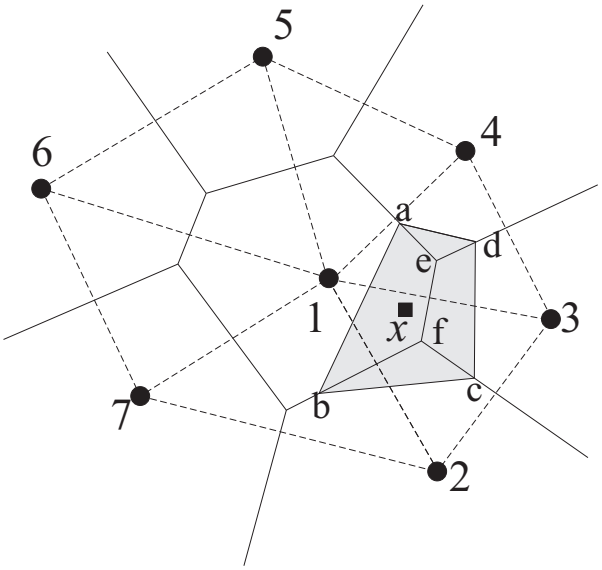

Figure 3. Modified Voronoi diagram by the inclusion of point $\boldsymbol{x}$

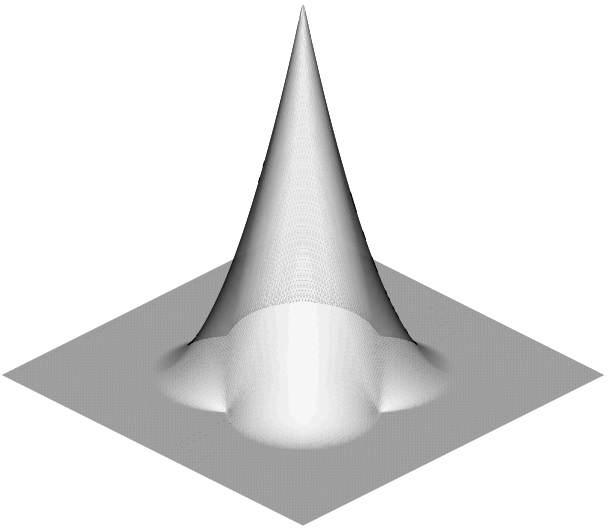

Figure 4. Sibson shape function. (Courtesy N. Sukumar)

It is a known fact [5] that the accuracy of many approximation methods is dependent on the regularity of the nodal distribution. As an example, the triangulation used in the FEM must comply with a minimum angle criterion in order to guarantee a minimum level of accuracy. However the NEM shape functions are not limited by such requirement, being independent of the nodal distribution. While this condition has not been formally demonstrated, studies in two [42] and in three [19] dimensions have not found any dependence between the angles of the Delaunay triangles and the accuracy of the obtained results, hence implying a meshless character, despite the existence of a triangulation. Indeed, in [1] numerical tests are performed that show the superior accuracy of NEM over FEM when highly distorted meshes are employed.

In addition, unlike most meshless methods, which are of approximate character, the NEM shape functions are strictly interpolant. That is, the approximated surface contains the nodal values. It

DOI: 10.1002/fld

satisfies the Kronecker delta condition at the nodes:

$$\phi_i(\boldsymbol{x}_j) = \delta_{ij} \tag{6}$$

As a consequence of this property, there is no need to use enforcing techniques to impose essential conditions while solving PDEs. However, this property alone is not sufficient to properly impose Dirichlet conditions, for the nodal satisfaction at the boundary nodes does not imply full compliance within the boundary.

Other interesting properties such as positivity, partition of unity, different degree of smoothness and consistency, etc. can be consulted in the bibliography [43] [19].

3. FREE SURFACE TREATMENT

The issue of dealing with the description of free surfaces deserves some comments. A particularly elegant analysis of the difficulties associated to an Eulerian/Lagrangian treatment of the equations arising from free surface flows can be found in [35]. Particularly noteworthy is the difficulty in the selection of mesh velocity in ALE formulations, in which the mesh moves with a velocity different to the material one, in order to minimize mesh distortion. Also, in Eulerian approaches, some marking technique should be used in order to track the evolution of the free surface. The Volume of Fluid (VoF) technique is an example of these techniques.

As stated before, meshless, or particle (those in which a mass is linked to each node) methods have avoided the need to perform such complicated treatments. Nevertheless, new difficulties arise. For instance, the nodal connectivity in meshless methods is not dictated by geometrical reasons (the best available triangle in terms of internal angles, for instance, in FE mesh generation) but by algorithmic reasons. In the Element Free Galerkin method [8], for instance, the connectivity is dictated primarily by the need of a support (radius of the shape function) big enough to encompass a sufficiently large number of nodes so as to make a matrix invertible. Remarkably, this is not related to the geometry of domain. That reason precludes the nodal connectivity to be used directly to determine the shape of the domain, as in FE methods. Nothing similar to an *isoparametric* representation exists in meshless methods.

Having made the choice of an updated Lagrangian description for the fluid kinematics, it is therefore necessary to somehow describe position of nodes at the free surface. The free-surface nature of the problem will surely lead to situations in which merging flows, breaking waves, splashing, etc. will occur. In these situations the algorithms to efficiently manage boundary markers become very intricate [35], especially in three dimensions.

Since the irruption of meshless methods, the possibility of employing techniques similar to those employed in three-dimensional scanning and reconstruction of solids become evident. [18] seems to have been the first work in employing *shape constructors* to this end. Since then, α-shapes have been widely employed in the context of meshless methods [19][37] [9] [32] [33] [27].

Different shape constructors have been proposed after α-shapes, see [11], [2], [3], [26] to name a few. In order to extract the geometry of the domain, in general, these methods propose a *filtration* of the Delaunay triangulation of the cloud of points. The Delaunay triangulation is the base ingredient of these techniques, since it characterizes unequivocally the cloud of points —it is unique for each cloud. For the NEM, in addition, it is a necessary ingredient already determined for shape function computation. Different criteria are proposed in order to select the triangles pertaining to the *shape* of the domain. The simplest one is maybe the α-shape technique, that proposes to eliminate all triangles (or tetrahedra) whose circumscribing radius (or, equivalently in finite element terminology, their associated mesh size, h) is greater than a prescribed *level of detail* for the geometry, α. Briefly speaking, α-shapes parametrize the finite-size family of shapes described by a nodal cloud by means of a parameter called α.

α-shapes have generated a great interest on "provable" shape reconstruction arguments. We mean that, under certain, usually very weak, assumptions on the size of the cloud of points, we obtain geometric and topologically accurate descriptions of the domain under consideration, see Fig. 5.

DOI: 10.1002/fld

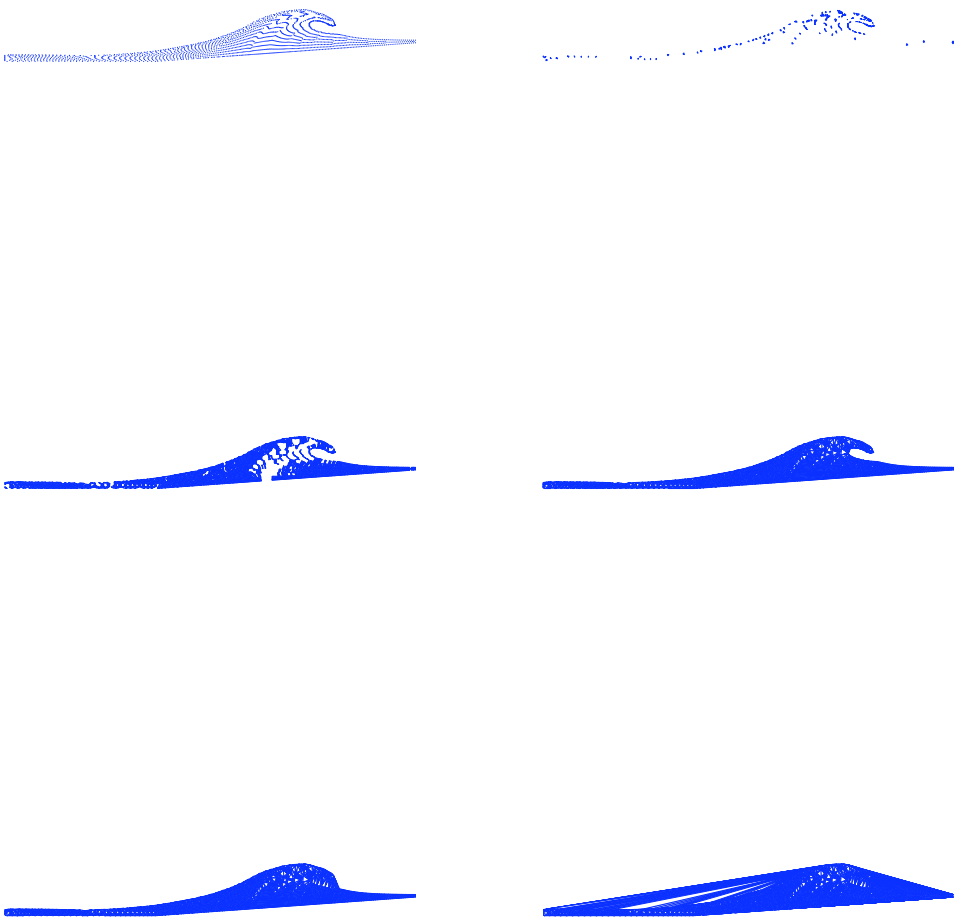

Figure 5. Evolution of the family of α-shapes of a cloud of points representing a wave breaking on a beach. Shapes $\mathcal{S}_0$ or cloud of points (a), $\mathcal{S}_{0.5}$ (b), $\mathcal{S}_{1.0}$ (c), $\mathcal{S}_{2.0}$ (d), $\mathcal{S}_{3.0}$ (e) and $\mathcal{S}_{\infty}$ (f) are depicted.

In [25] the authors presented a technique, well suited for the numerical simulation of free-surface flows, that avoids some previous problems of standard α-shapes. These problems arose notably in situations such as merging flows, breaking waves, etc., in which contact between free surfaces is detected in advance to the real occurrence. The proposed technique is based in performing an additional filtration to the Delaunay triangulation (tetrahedrization) of the cloud of points. After the α-filtration, we perform an additional filtration based on the information provided by nodal velocities at the last converged time step, and the gradient of velocities. The tests performed during these works have provided excellent results over problems where traditional α-shapes have revealed deficiencies.

DOI: 10.1002/fld

4. GOVERNING EQUATIONS

In this section, the conservation equations are developed to arrive at the Navier-Stokes equations. We begin by considering here the flow of an incompressible viscous fluid, although some form of non-Newtonian fluid will be considered later on. In this kind of problems, the non linear convective terms mentioned are usually a source of numerical problems if an Eulerian or ALE approach is chosen. Since a Lagrangian scheme is employed in our method, these terms will not appear in the equations, making it unnecessary any kind of stabilisation.

4.1. Conservation Equations

For the development of the governing equations, we consider a fluid occupying a region Ω in $\Re^2$ or $\Re^3$, although in general we will say it occupies a volume V. The fluid presents a density ρ and a dynamic viscosity μ.

4.1.1. Mass Conservation Following standard assumptions, the conservation of mass through time in a given volume, assuming no mass is added or destroyed, is given by

$$\frac{d\rho}{dt} + \rho\nabla\cdot\boldsymbol{v} = 0 \tag{7}$$

4.1.2. Momentum Conservation Now, let we assume that the fluid particles are subjected to tensional state $\boldsymbol{\sigma}$ and distributed body forces $\rho\boldsymbol{b}$. The linear momentum conservation principle states that the time variance of linear momentum equals the sum of all forces acting on the body, that is

$$\rho\frac{d\boldsymbol{v}}{dt} + \rho(\boldsymbol{v}\cdot\nabla)\boldsymbol{v} = \rho\boldsymbol{b} + \nabla\cdot\boldsymbol{\sigma} \quad \text{or} \quad \frac{d\rho\boldsymbol{v}}{dt} = \rho\boldsymbol{b} + \nabla\cdot(\boldsymbol{\sigma} + \rho\boldsymbol{v}\otimes\boldsymbol{v}). \tag{8}$$

4.2. Constitutive equations for a Newtonian fluid

Fluids are characterized for a continuous deformation under shear stresses and for as long as the stresses act. As a by-product of this property, resting fluids cannot undergo any shear stress at all. Therefore, the constitutive equation for a Newtonian fluid will be

$$\boldsymbol{\sigma} = -p\boldsymbol{I} + 2\mu\nabla^s\boldsymbol{v} \tag{9}$$

which is known as Stokes' law.

4.3. Navier-Stokes Equations

The laminar flow of fluids subject to external and body forces can be described by solving the conservation equations coupled with a given constitutive relationship. To formally enunciate the Navier-Stokes problem we will consider a closed finite fluid domain Ω in $\Re^n$ with $n = 2$ or 3 and a closed and sufficiently regular boundary $\Gamma = \partial\Omega$. The time-dependent flow of an incompressible viscous fluid must follow

$$\rho(\boldsymbol{v}_{,t} + (\boldsymbol{v}\cdot\nabla)\boldsymbol{v}) = \nabla\cdot\boldsymbol{\sigma} + \rho\boldsymbol{b} \quad \text{in}\,\Omega\times(0,T), \tag{10}$$

$$\nabla\cdot\boldsymbol{v} = 0 \quad \text{in}\,\Omega\times(0,T) \tag{11}$$

$$\boldsymbol{v}(\boldsymbol{x},t) = \boldsymbol{v}_D(\boldsymbol{x},t), \quad \boldsymbol{x}\in\Gamma_D, \quad t\in(0,T) \tag{12}$$

$$\boldsymbol{n}\cdot\boldsymbol{\sigma}(\boldsymbol{x},t) = \boldsymbol{t}(\boldsymbol{x},t), \quad \boldsymbol{x}\in\Gamma_N, \quad t\in(0,T) \tag{13}$$

Eq. (11) is the incompressibility condition and implies that the elements of the fluid do not suffer any change in density when subjected to pressure changes.

Prepared using fldauth.cls
DOI: 10.1002/fld

4.4. Weak Formulation

To recall, we are treating with the dynamic response of incompressible viscous fluids described by

$$\boldsymbol{\nabla} \cdot \boldsymbol{\sigma} + \rho \boldsymbol{b} = \rho \left(\frac{\partial \boldsymbol{v}}{\partial t} + \boldsymbol{v} \cdot \boldsymbol{\nabla} \boldsymbol{v} \right) = \rho \frac{d\boldsymbol{v}}{dt}, \tag{14}$$

$$\boldsymbol{\nabla} \cdot \boldsymbol{v} = 0, \tag{15}$$

$$\boldsymbol{\sigma} = -p\boldsymbol{I} + 2\mu \nabla^s \boldsymbol{v} = -p\boldsymbol{I} + \boldsymbol{T} \tag{16}$$

After introducing the constitutive equation, Eq. (16), in the momentum conservation equation, Eq. (14), multiplying by a suitable test function, and integration in the whole domain Ω, we obtain

$$\int_\Omega 2\mu \boldsymbol{D} : \boldsymbol{D}^* d\Omega - \int_\Omega p\boldsymbol{I} : \boldsymbol{D}^* d\Omega = -\int_\Omega \rho \boldsymbol{b} \boldsymbol{v}^* d\Omega + \int_\Omega \rho \frac{d\boldsymbol{v}}{dt} \boldsymbol{v}^* d\Omega, \tag{17}$$

$$\int_\Omega \boldsymbol{\nabla} \cdot \boldsymbol{v} p^* d\Omega = 0 \tag{18}$$

where $\boldsymbol{D} = \nabla^s \boldsymbol{v}$ represents the strain rate tensor and $\boldsymbol{b}$ are the body forces. The test functions are $\boldsymbol{v}^*$ and p^* which correspond to the different essential variables, namely: the velocity and pressure.

5. TIME DISCRETISATION

The convective terms of Eq. (8) were replaced by a Lagrangian time derivative, which is a material derivative along the fluid's particles trajectory. This term, the second in the r.h.s. of Eq. (17), gathers the inertial effects of the flow. Using a standard first-order finite difference time discretisation along the particle's path, and knowing the solution at time $t^{n-1} = (n-1)\Delta t$, we can calculate the solution at $t^n = n\Delta t$ by means of

$$\int_\Omega \rho \frac{d\boldsymbol{v}}{dt} \boldsymbol{v}^* d\Omega = \int_\Omega \rho \frac{\boldsymbol{v}^n(\boldsymbol{x}) - \boldsymbol{v}^{n-1}(\boldsymbol{X}(t^{n-1}))}{\Delta t} \boldsymbol{v}^* d\Omega, \tag{19}$$

In this equation $\boldsymbol{X}(t)$ represents the position at time t along the characteristic line that passes through point $\boldsymbol{x}$ at time t^n, so $\boldsymbol{X}(t^{n-1})$ is the position the material particle occupied during the last time step. For an even simpler notation, we will denote this point as $\boldsymbol{X}_{n-1}$. Using this notation the particle position can be written as

$$\boldsymbol{x} = \boldsymbol{X}_{n-1} + \boldsymbol{v}^{n-1}(\boldsymbol{X}_{n-1}) \Delta t \tag{20}$$

This was the temporal discretisation employed in [27]. With it, the weak form of the Navier-Stokes equations is

$$\int_\Omega 2\mu \boldsymbol{D} : \boldsymbol{D}^* d\Omega - \int_\Omega p\boldsymbol{I} : \boldsymbol{D}^* d\Omega - \int_\Omega \rho \frac{\boldsymbol{v}\boldsymbol{v}^*}{\Delta t} = -\int_\Omega \rho \boldsymbol{b} \boldsymbol{v}^* d\Omega - \int_\Omega \rho \frac{\boldsymbol{v}^{n-1}\boldsymbol{v}^*}{\Delta t} d\Omega, \tag{21}$$

$$\int_\Omega \nabla \cdot \boldsymbol{v} p^* d\Omega = 0 \tag{22}$$

This scheme produces accurate results for some problems [27], while for others, as will be demonstrated next, gives poor results. When a more accurate scheme is needed, it is possible to employ a second-order time discretisation in the same framework. In [10] it is shown that a higher order time discretisation not only increases accuracy but also relaxes the spatial-temporal restrictions imposed by the CFL conditions. In this work a second-order in time approach has been then employed:

$$\int_\Omega \rho \frac{d\boldsymbol{v}}{dt} \boldsymbol{v}^* d\Omega = \int_\Omega \rho \frac{3\boldsymbol{v}^n(\boldsymbol{x}) - 4\boldsymbol{v}^{n-1}(\boldsymbol{X}(t^{n-1})) + \boldsymbol{v}^{n-2}(\boldsymbol{X}(t^{n-2}))}{2\Delta t} \boldsymbol{v}^* d\Omega, \tag{23}$$

DOI: 10.1002/fld

leaving the weak form of the problem as

$$\int_\Omega 2\mu \boldsymbol{D} : \boldsymbol{D}^* d\Omega - \int_\Omega p\boldsymbol{I} : \boldsymbol{D}^* d\Omega - \frac{3}{2}\int_\Omega \rho \frac{\boldsymbol{v}\boldsymbol{v}^*}{\Delta t} =$$
$$-\int_\Omega \rho \boldsymbol{b}\boldsymbol{v}^* d\Omega - 2\int_\Omega \rho \frac{\boldsymbol{v}^{n-1}\boldsymbol{v}^*}{\Delta t} d\Omega + \frac{1}{2}\int_\Omega \rho \frac{\boldsymbol{v}^{n-2}\boldsymbol{v}^*}{\Delta t}, \tag{24}$$

$$\int_\Omega \nabla \cdot \boldsymbol{v} p^* d\Omega = 0 \tag{25}$$

Note that in the weak form equations, the past velocities have been written as $\boldsymbol{v}^{n-i}$ but they are still evaluated at points $\boldsymbol{X}_{n-i}$.

5.1. Algorithmic Issues

The most difficult terms to evaluate in Eq. (21) or Eq. (24) are those which refer to the particle position at past times. The numerical integration of this terms depends on the quadrature scheme employed. If we employ traditional Gauss-based quadratures on the Delaunay triangles, it will be necessary to find the position at time t^{n-1} (and at t^{n-2}) of the material particle now (at time t^n) occupying the position of the integration point in question.

To explain this problem and the employed solution method, we will refer to the first order time discretisation, Eq. (21). The integration of the term in question is performed according to

$$\int_\Omega \rho \frac{\boldsymbol{v}^{n-1}\boldsymbol{v}^*}{\Delta t} d\Omega = \sum_k \rho \frac{\boldsymbol{v}^{n-1}(\boldsymbol{\Xi}_k)\boldsymbol{v}(\boldsymbol{\xi}_k)}{\Delta t} w_k, \tag{26}$$

where w_k represents the weight associated to integration point k. That point occupies the position $\boldsymbol{\xi}_k$ at the current time instant, and the characteristic line $\boldsymbol{X}(\boldsymbol{\xi}_k, t^n; t)$ passes through $\boldsymbol{\Xi}_k$ at t^{n-1}.

Two main difficulties need to be addressed: finding $\boldsymbol{\Xi}_k$ and evaluating $\boldsymbol{v}^{n-1}(\boldsymbol{\Xi}_k)$. The later may be performed by interpolation between neighbouring nodes, given that the past nodal velocities are stored, which is fairly easy to assure. It is also necessary to know which nodes were near $\boldsymbol{\Xi}$, so we it is assumed that the nodal connectivity remains constant within two consecutive time increments. Although this is known to be false, in general, it is a reasonable assumption for small time increments. It would be more accurate to store and manipulate all the information regarding nodal connectivity for past steps, but the possible gains do not compensate the computational costs in the cases where that is even possible —closed codes could probably deny that possibility at all. It can occur that some of the nodes neighbouring the integration point at time t were not actually its neighbours at time t^{n-1}, but this does not constitute a problem, since the number of natural neighbours of a point is usually high (much more than three), so the quality of the interpolation is thus guaranteed.

Regarding the search for $\boldsymbol{\Xi}$, we utilize a two-step iterative procedure. Firstly the integration point $\boldsymbol{\xi}$ is projected backwards in time by

$$\boldsymbol{\Xi}_i = \boldsymbol{\xi} - \boldsymbol{v}^{n-1}(\boldsymbol{\Xi}_{i-1})\Delta t, \tag{27}$$

for the first iteration the past velocities of the neighbouring nodes are evaluated at t^n to make the projection.

In the second step, the velocity $\boldsymbol{v}^{n-1}(\boldsymbol{\Xi}_i)$ is evaluated and then the projection in t^n of $\boldsymbol{\Xi}_i$ is computed

$$\boldsymbol{\xi}_i = \boldsymbol{\Xi}_i + \boldsymbol{v}^{n-1}(\boldsymbol{\Xi}_i)\Delta t \tag{28}$$

iteratively until $\boldsymbol{\xi} \approx \boldsymbol{\xi}_i$. [27] reports convergence in two or three iterations with an error of the order of 10^{-8}.

When employing a second-order time discretisation, the process will be performed in a recursive way, solving for the t^{n-1} and t^{n-2} time steps. In this case

$$\boldsymbol{\Xi} = \boldsymbol{\Xi}' + \boldsymbol{v}^{n-2}(\boldsymbol{\Xi}')\Delta t \tag{29}$$

$$\boldsymbol{\xi} = \boldsymbol{\Xi}' + \boldsymbol{v}^{n-2}(\boldsymbol{\Xi}')\Delta t + \boldsymbol{v}^{n-1}(\boldsymbol{\Xi})\Delta t \tag{30}$$

Prepared using fldauth.cls
DOI: 10.1002/fld

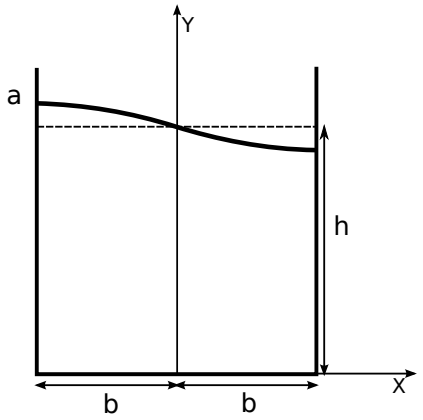

Figure 6. Initial configuration for a 2-D sloshing problem.

where $\Xi' = \boldsymbol{X}(\boldsymbol{\xi}, t^n; t^{n-2})$ represents the root of the characteristic line passing through $\boldsymbol{\xi}$, at time t^{n-2}.

If some type of nodal integration is employed, as in [12] or [31], this procedure becomes unnecessary as it is only necessary to store nodal velocities at time steps t^{n-1} and t^{n-2}.

5.2. Numerical example: Sloshing

The first-order version of this formulation has been tested in [27] for Newtonian fluids and has shown a very good performance in the simulation of free surface flows. We refer the reader to these works for more details on the topic. However, it has also demonstrated problems, and very often lack of convergence in the characteristic root finding, when applied to fluid-structure interaction problems. In this section the behaviour of the higher-order time discretisation in a situation where the original formulation was unable to yield appropriate results is shown.

A two-dimensional sloshing problem with small deformations as proposed in [40] is considered. The initial setting is shown in Fig. 6. In this problem a stationary fluid in an unstable initial condition is set free to move under the gravity influence alone. The fluid is contained in a two-dimensional tank. The goal is to determine the wave amplitude in time.

The initial surface elevation is given by

$$\eta_o = a \; cos \; k_2(x + l/2) \tag{31}$$

with

$$k_n = n\pi/l \tag{32}$$

where n represents the number of waves present in a tank of with l. a represents the initial maximum amplitude measured from the mean level h.

An analytical solution was proposed by Prosperetti [39] for certain parameters for which is possible to obtain a solution for the amplitude. In this case the solution is given by

$$a(t) = \frac{4v^2k^4}{8v^2k^4 + w_0^2} a_0 erfc\left(\sqrt{vk^2 t}\right) + \sum_{i=1}^{4} \frac{z_i}{Z_i} \left(\frac{w_0^2 a_0}{z_i^2 - vk^2}\right) exp[(z_i^2 - vk^2)t] erfc(z_i\sqrt{t}), \tag{33}$$

where a_0 is the initial amplitude, w_0 is the natural inviscid frequency: $w_0^2 = gk + \gamma k^3$; the z_i are the four roots of

$$z^4 + 2k^2 v z^2 + 4(k^2 v^3)^{3/2} + v^2 k^4 + w_0^2 = 0 \tag{34}$$

DOI: 10.1002/fld

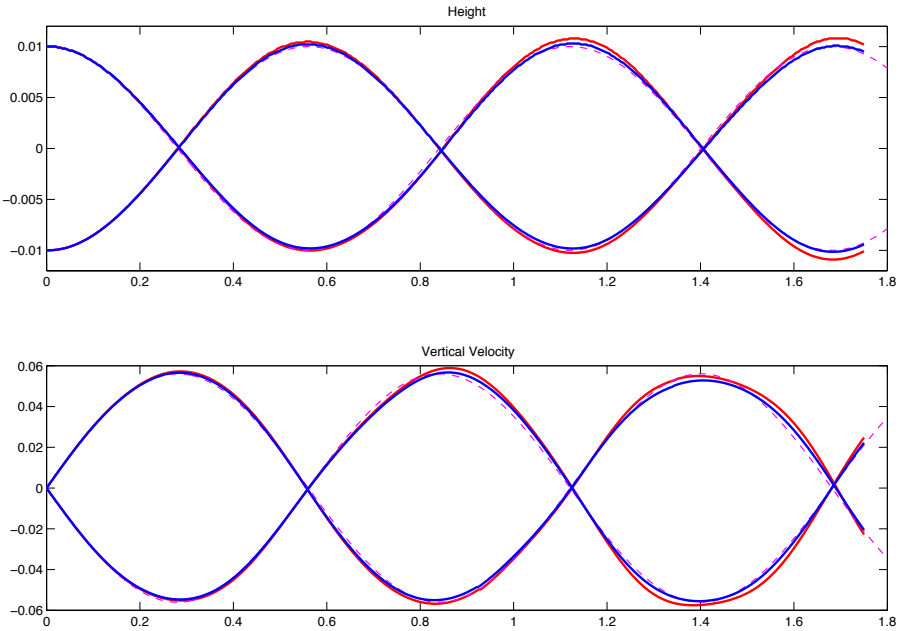

Figure 7. Vertical displacement and velocities at both edges of the free surface. The second-order solution is shown in blue, the first-order solution in red and the analytic solution in purple, discontinuous line. Notice how the first-order solution diverges from the very first cycles of the oscillation.

and $Z_1 = (z_2 - z_1)(z_3 - z_1)(z_4 - z_1)$. Z_2, Z_3, Z_4 are obtained by a permutation of the indices.

Free-slip conditions were imposed along the tank walls. Note there is no need to impose conditions on the free surface, nor to perform any special boundary tracking of it.

For discretisation purposes, Sibson approximation was chosen for the velocity field, whereas piece-wise constant (Thiessen) approximation was chosen for the pressure. This kind of approximation is known not to fulfil the inf-sup condition associated with the incompressibility condition, see [28], but nevertheless still provides with stable results in the vast majority of cases, very rarely producing volumetric locking. This is the reason why an as much simple as possible approach has been preferred.

In the shown case a time increment $\Delta t = 0.005s$ was used. The Reynolds number resulted to be of 3200. The gravity force had an acceleration of $g = 9.8\ m/s^2$.

In Fig. 7 both first-order and-second order schemes can be compared. With an amplified vertical axis it is possible to notice how the first order scheme was unable to replicate the diminishing amplitude of the oscillations. At larger time increments the solution even diverges, while the second order scheme was able to still give reliable results.

In Figs. 8 to 10 the velocity field for different time steps is shown. Vectors show the direction of the velocity, while the colours show its magnitude.

By incorporating more historical information about the previous flow steps, it was possible to reduce error and reach better approximations. The improved accuracy comes at a cost of increased resource requirements (CPU time, memory and storage) but nevertheless the increase is not in general excessive. The characteristic root finding algorithm has shown to converge in a very reduced number of iterations (2-3) for the vast majority of cases tested.

DOI: 10.1002/fld

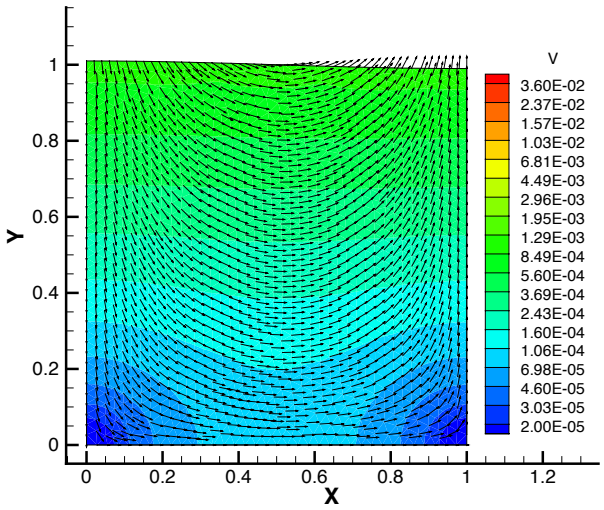

Figure 8. Velocity field at time $t = 0.005$.

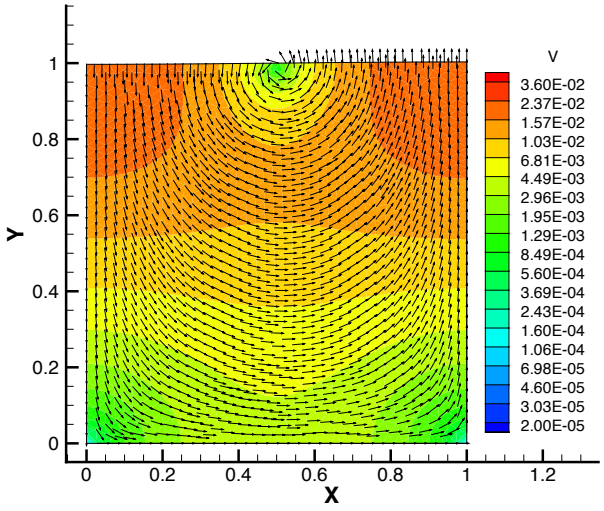

Figure 9. Velocity field at time $t = 0.455$.

6. APPLICATION TO NON-NEWTONIAN FLUIDS: THE OLDROYD B MODEL

In 1950, Oldroyd developed a constitutive equation that, while simple, is useful in describing the general flow behaviour of dilute polymeric solutions. This model can be obtained as an empirical generalization of the linear viscoelastic equation.

DOI: 10.1002/fld

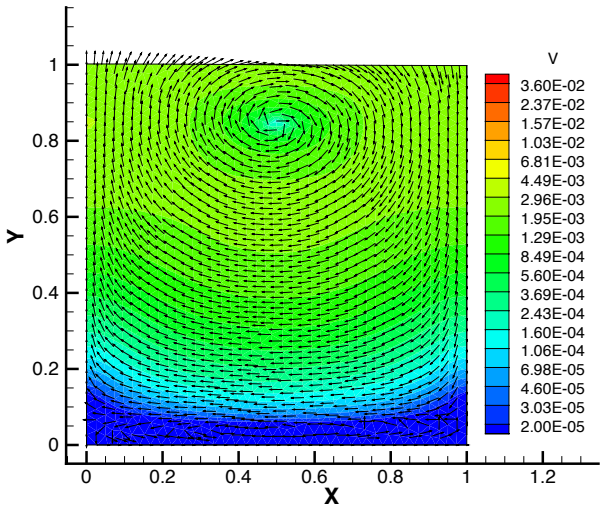

Figure 10. Velocity field at time $t = 1.205$.

Another —and probably more popular—way to derive this model is to consider a suspension of Hookean dumbbells in a Newtonian solvent and study it from a molecular point of view [38]. These dumbbells represent the polymer chains suspended in the Newtonian medium. They will react to the flow and to other dumbbells, and will add some extra resistance to the viscous character of the solvent. When the fluid stops the springs will remember their initial configuration, hence representing the elastic component of the model. Probably the most interesting part about this approach, is the way to obtain a somewhat accurate macroscopic model based on molecular assumptions.

The Oldroyd B model presents a constant shear viscosity very much like that observed on Bogger fluids [38], which are highly elastic non-shear thinning fluids. Still, this model is useful only at low shear rates. In extensional flows, the infinite extensibility of the hookean springs in the dumbbells yield an extensional viscosity that tends to infinity at a finite extensional rate. To appreciate the challenges associated with the simulation of Oldroyd B-type fluids, the interested reader is referred to [48]. Free-surface phenomena, in addition, very much complicates the problem.

The constitutive equation for Oldroyd B-type fluids is given by

$$\boldsymbol{T} + \lambda_1 \overset{\nabla}{\boldsymbol{T}} = \eta_0 \left(\dot{\boldsymbol{\gamma}} + \lambda_2 \overset{\nabla}{\dot{\boldsymbol{\gamma}}} \right), \tag{35}$$

where $\boldsymbol{T}$, the deviatoric part of the stress tensor $\boldsymbol{\sigma}$, is known as the extra-stress tensor and the triangle denotes the non-linear upper-convected derivative introduced by Oldroyd [48]. The coefficients η_0, λ_1 and λ_2 are material constants. Finally, following standard notation, $\dot{\boldsymbol{\gamma}} = (\boldsymbol{\nabla}^s \boldsymbol{v}) = \boldsymbol{D}$ represents the strain rate tensor.

We now separate the stress in the solvent (denoted by a subscript s) and polymeric (denoted by a subscript p) components as

$$\boldsymbol{T} = \eta_s \dot{\boldsymbol{\gamma}} + \boldsymbol{\tau}, \tag{36}$$

and substitute into Eq. (35) to get

$$\boldsymbol{\tau} + \lambda_1 \overset{\nabla}{\boldsymbol{\tau}} = \eta_p \dot{\boldsymbol{\gamma}}, \tag{37}$$

DOI: 10.1002/fld

which is the constitutive equation for the elastic stress. It is possible to note from this equation that there is no need to solve the Fokker-Plank equation related to the molecular description of Oldroyd B models in order to find the extra-stresses. When $\eta_s \to 0$, $\boldsymbol{T} \equiv \boldsymbol{\tau}$ and this model reduces to the Upper Convected Maxwell Model.

6.1. Model Implementation

Let us recall the Navier-Stokes problem,

$$\rho(\boldsymbol{v}_{,t} + (\boldsymbol{v} \cdot \nabla)\boldsymbol{v}) = \nabla \cdot \boldsymbol{\sigma} + \rho \boldsymbol{b} \quad \text{in } \Omega \times (0,T), \tag{38}$$

$$\nabla \cdot \boldsymbol{v} = 0 \quad \text{in } \Omega \times (0,T) \tag{39}$$

$$\boldsymbol{v}(\boldsymbol{x},t) = \boldsymbol{v}_D(\boldsymbol{x},t), \quad \boldsymbol{x} \in \Gamma_D, \quad t \in (0,T) \tag{40}$$

$$\boldsymbol{n} \cdot \boldsymbol{\sigma}(\boldsymbol{x},t) = \boldsymbol{t}(\boldsymbol{x},t), \quad \boldsymbol{x} \in \Gamma_N, \quad t \in (0,T), \tag{41}$$

and introduce the Oldroyd B constitutive equation. Equation (38) will change to

$$\rho(\boldsymbol{v}_{,t} + (\boldsymbol{v} \cdot \nabla)\boldsymbol{v}) = \nabla \cdot \boldsymbol{\sigma}_n + \nabla \boldsymbol{\tau} + \rho \boldsymbol{b}, \tag{42}$$

where $\boldsymbol{\sigma}_n$ denotes the Newtonian component of the stress: $-p\boldsymbol{I} + \eta_s \dot{\boldsymbol{\gamma}}$.

We expand now the upper convected derivative in Eq. (37) to get

$$\boldsymbol{\tau} + \lambda_1 \left(\frac{D\boldsymbol{\tau}}{Dt} - (\nabla \boldsymbol{u})^T \boldsymbol{\tau} - \boldsymbol{\tau} (\nabla \boldsymbol{u}) \right) = \eta_p \dot{\boldsymbol{\gamma}}, \tag{43}$$

from which

$$\frac{D\boldsymbol{\tau}}{Dt} = \frac{\eta_p \dot{\boldsymbol{\gamma}} - \boldsymbol{\tau}}{\lambda_1} + (\nabla \boldsymbol{u})^T \boldsymbol{\tau} + \boldsymbol{\tau} (\nabla \boldsymbol{u}) \tag{44}$$

where a first-order time discretisation for the elastic part of the stress tensor has been employed

$$\frac{D\boldsymbol{\tau}}{Dt} = \frac{\boldsymbol{\tau}^n + \boldsymbol{\tau}^{n-1}}{\Delta t}. \tag{45}$$

In the implementation here developed it is assumed that the extra-stress at $t = t_{n-1}$ is known, so when solving for $\boldsymbol{u}|_{t=n}$ all terms in Eq.(42) are known. After the velocity field has been obtained, the velocity derivatives, which are known for the integration points, are projected to the nodes (this intermediate step is by no means necessary if Stabilized Conforming Nodal Integration [31] [12] is used). This intermediate variable along with $\boldsymbol{\tau}_{n-1}$ is used to calculate $\boldsymbol{\tau}_{n+1}$ according to

$$\boldsymbol{\tau}^n = \boldsymbol{\tau}^{n-1} + \Delta t \left(\frac{\eta_p \dot{\boldsymbol{\gamma}}^{n-1} - \boldsymbol{\tau}^{n-1}}{\lambda_1} + \left(\nabla \boldsymbol{u}^{n-1}\right)^T \boldsymbol{\tau}^{n-1} + \boldsymbol{\tau}^{n-1} \left(\nabla \boldsymbol{u}^{n-1}\right) \right). \tag{46}$$

Notably, if the method here presented is compared to that of [46], or in general any based upon finite difference or finite volume schemes, it must be highlighted that no special treatment is necessary to compute the stress tensor along the boundaries.

7. NUMERICAL EXAMPLES

In order to demonstrate the method's ability to reproduce the motion of non-Newtonian flows we simulated an extrusion process which causes the *die swelling* effect, on one hand, and the impact of a splashing drop on the other. Each problem has been studied by many authors and almost constitute a benchmark for the simulation of non-Newtonian flows in the presence of free surfaces.

DOI: 10.1002/fld

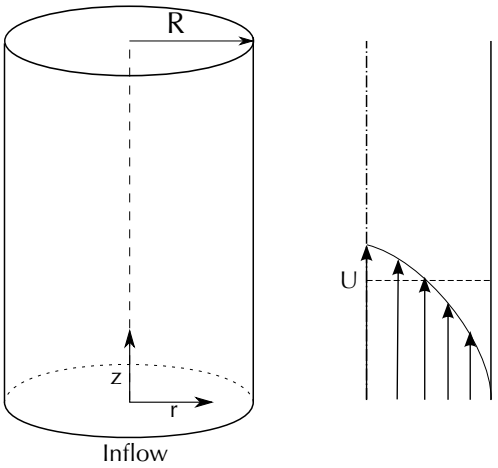

Figure 11. Flow schematics

7.1. Model Validation: Fully developed flow Inside a Pipe

Aiming at checking the accuracy of the proposed technique, a developed flow was simulated inside a completely full pipe of length L and radius $R = 1$. In this case an axisymmetric representation of the problem with the symmetry axis set on $x = 0$ was employed.

On the Pipe walls ($r = R$) a no-slip boundary condition was applied ($v_r = v_z = 0$) while no special outflow conditions are necessary. Any particle that crossed the boundary set on $z = L$, was eliminated from the simulation. Similarly, the flow is forced by entering a set of particles through the inflow boundary. At the entrance, velocity conditions were those of a fully developed flow, that is,

$$v_r = 0 \tag{47}$$

$$v_z = \frac{2U(R^2 - r^2)}{R^2} \tag{48}$$

where U is the average velocity.

Two non-dimensional numbers are widely used to characterize the flow of non-Newtonian fluids. The first is the Reynolds number Re, defined as

$$Re = \frac{\rho_0 U L}{\mu_0}, \tag{49}$$

and

$$We = \frac{\lambda_0 U}{L} \tag{50}$$

which is called the Weissenberg number. This dimensionless number is the ratio of the relaxation time of the fluid and a specific process time and represents a non-dimensional measure of the fluid's elasticity.

Since the non Newtonian behaviour depends on the history of the flow and we assume that the particles are already moving at $t < 0$, in order to fix the initial boundary conditions it is necessary for each of them to know their past extra-stress tensor. For this reason the initial velocity and stress condition in all the domain were imposed in the same way as is done at the inflow boundary.

For a node cloud composed initially by 3999 nodes (remember that the simulation is left until the steady-state is reached, while nodes enter and leave the domain through the inflow and outflow boundaries), the solution was stable from the first step, and after 500 time steps, the extra-stress field was as shown in Figs. 12 and 13. The τ_{xx} component is not shown here because it vanishes for the whole domain.

DOI: 10.1002/fld

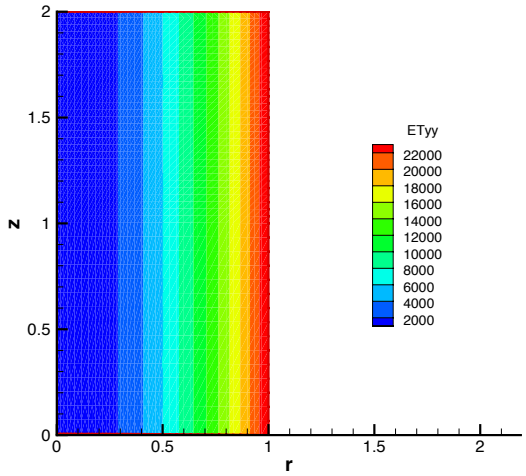

Figure 12. Extra-stress field for a fully developed pipe flow: τ_{yy}

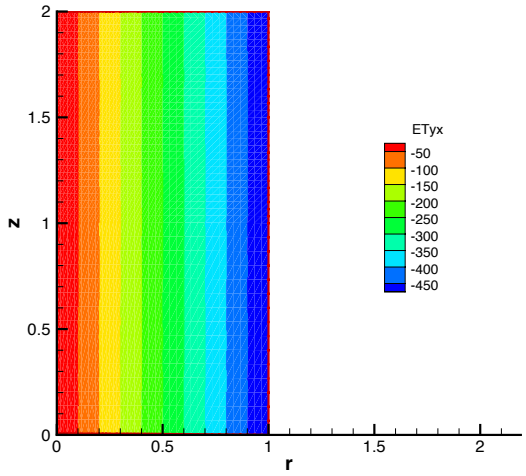

Figure 13. Extra-stress field for a fully developed pipe flow: τ_{xy}

As can be noticed in Figs. 14 through 16, where the analytical solution for τ_{xy}, τ_{yy} and $\boldsymbol{v}_y$ is shown by a red line; the agreement between the expected behaviour and the results obtained is remarkable. The $\mathcal{L}_2$-norm of the errors are $Err_{\tau_{xy}} = 6.3027 \cdot 10^{-06}$, $Err_{\tau_{yy}} = 1.4730 \cdot 10^{-06}$ and $Err_{V_y} = 2.3987 \cdot 10^{-07}$.

7.2. Die Swelling

A visco-elastic fluid jet presents a characteristic behaviour known as *extrudate swell* that consist in the jet expansion in the direction perpendicular to the stream after leaving the extrusion die. This phenomenon is also known as *die swelling*. It is a very important effect in the polymer industry

DOI: 10.1002/fld

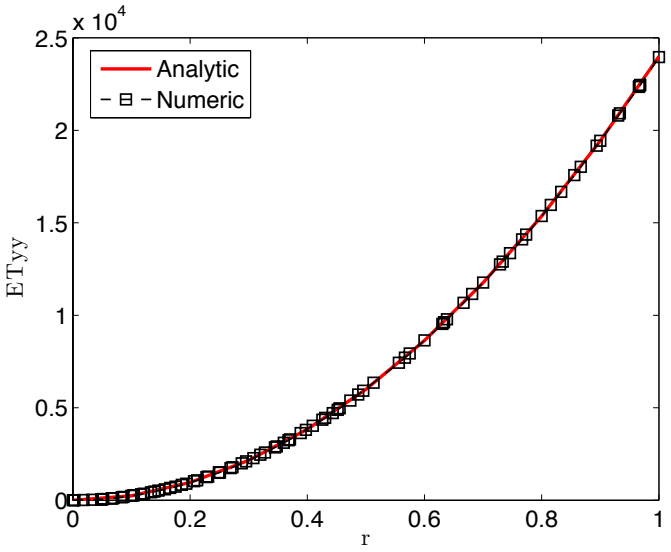

Figure 14. Extra-stress field for a fully developed pipe flow: τ_{yy} at $y = 1$

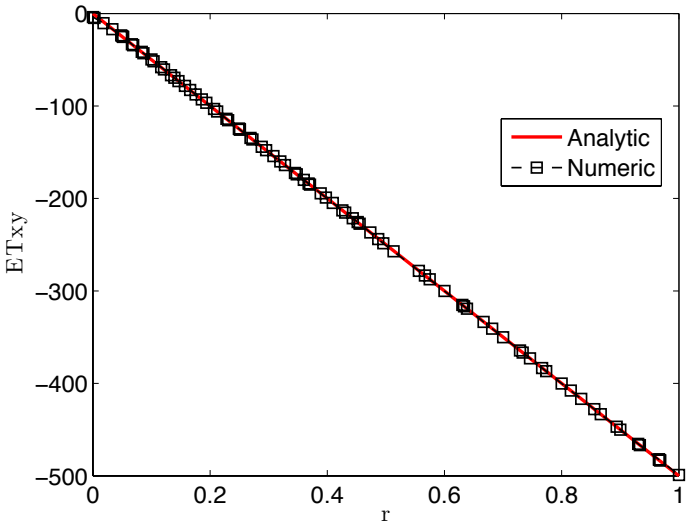

Figure 15. Extra-stress field for a fully developed pipe flow: τ_{xy} at $y = 1$

because many processes involve the extrusion of viscoelastic fluids, for example plastic in their molten state. The phenomenon of die swell may be explained by elastic recovery. The molecules are stretched by the shear forces in the pipe and the average axial stress at the exit is a tension.

In this problem we simulated the exit of an Oldroyd B fluid trough a circular extrusion die of radius R and length L. The swell ratio S_r, which is defined as the ratio of the maximum diameter of the jet and the diameter of the die, was measured as a way to quantify the swelling effect.

The problem set-up is similar to the pipe flow, a fully developed flow passes through a pipe which imposes a no-slip condition to the particles in contact with it as in the previous example. The only difference is that the pipe has a finite length, that in this case causes all nodes reaching the end of the pipe to be free of any condition. Gravity and inertial effects were neglected.

DOI: 10.1002/fld

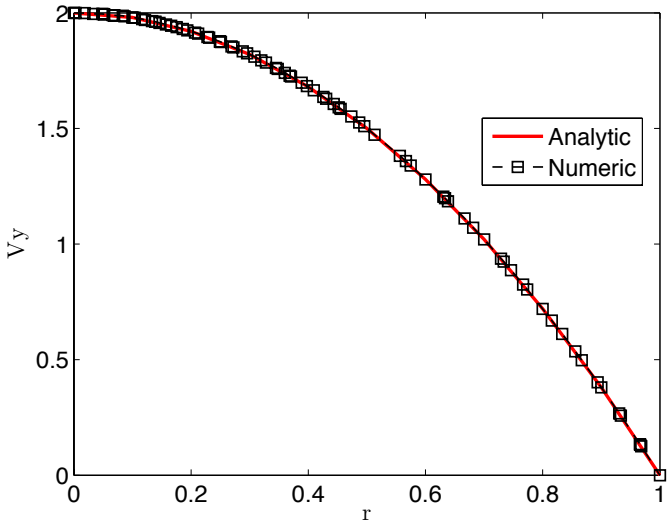

Figure 16. Velocity profile for a fully developed pipe flow: $\boldsymbol{V}_y$ at $y = 1$

Following the steps of [46], different flows were simulated with the following parameters: $R = 0.1m$, $U = 1m/s$, $\mu_0 = 0.01m^2s^{-1}$ and $\lambda_1 = 0.01$. The scaling parameters were R, U, μ_0 and λ_1. Therefore $Re = 1$ and $We = 1$. The ratio λ_2/λ_1 took values of 0 (Newtonian case), 0.1, 0.5, 0.7 and 0.9. The effective Weissenberg number, defined as

$$We_{ef} = \left(1 - \frac{\lambda_2}{\lambda_1}\right) We, \tag{51}$$

was therefore $We_{ef} = 0.9, 0.5, 0.3$ and 0.1.

The swelling ratios obtained were lower than those obtained by Tomé [46], who reported values of $S_r = 2.13, 1.88$ and 1.37 for $We_{ef} = 0.9, 0.5$ and 0.1. Our model resulted in $S_r = 1.504, 1.435, 1, 236$ and 1.133 for $We_{ef} = 0.9, 0.5, 0.3$ and 0.1 respectively. Figure 17 presents the fluid contours at a point at which the die swelling for each fluid has already stabilized. It is possible to notice the deviation from the Newtonian behaviour as We increases.

In a later section of the same work [46], a comparison is made against the works of Crochet [16] and an analytical solution to this problem by Tanner [45]. These tests allow to check the proposed method in a more meaningful way. In his work, Tanner used the *recoverable shear* which is a non-dimensional number defined as

$$S_R = \frac{\tau_{zz}}{2\left[\tau_{rz} + \frac{2\lambda_2}{Re\lambda_1}\dot{\gamma}_{rz}\right]}, \tag{52}$$

evaluated at the pipe wall.

Since the flow is fully developed inside the pipe, we use Eqs. (47) and (48) so the relevant terms in equation (52) in their non-dimensional form are

$$\begin{aligned}
\tau_{zz} &= 2We\tau_{rz}\frac{\partial v_z}{\partial r}, \\
\tau_{rz} &= \frac{1}{Re}\left(1 - \frac{\lambda_2}{\lambda_1}\right)\frac{\partial v_z}{\partial r}, \\
\dot{\gamma}_{rz} &= \frac{1}{2}\frac{\partial v_z}{\partial r}.
\end{aligned}$$

DOI: 10.1002/fld

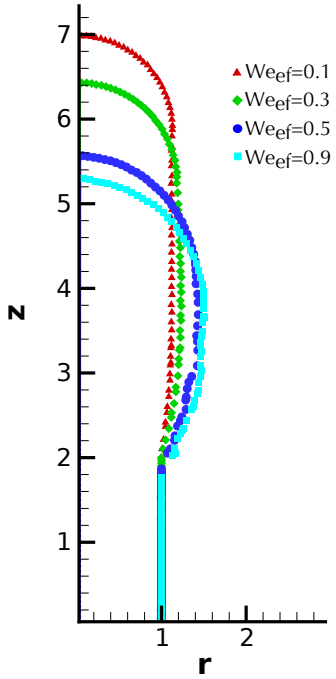

Figure 17. Swelling comparison between fluids with different Weissenberg numbers

thus

$$S_R = \frac{2We\tau_{rz}(\partial v_z/\partial r)}{2\left[\frac{1}{Re}\left(1-\frac{\lambda_2}{\lambda_1}\right)\frac{\partial v_z}{\partial r}+\frac{1}{Re}\left(\frac{\lambda_2}{\lambda_1}\right)\frac{\partial v_z}{\partial r}\right]} = We\left(1-\frac{\lambda_2}{\lambda_1}\right)\frac{\partial v_z}{\partial r},$$

and since in this case

$$\left|\frac{\partial v_z}{\partial r}\right|_{r=\pm R} = 4 \implies S_R = 4\left(1-\frac{\lambda_2}{\lambda_1}\right)We$$

The theoretic swelling ratio S_r of an axisymmetric jet can be predicted in a simplified manner via the equation [45]

$$\frac{D_{max}}{D} = 0.14 + \left[1+\frac{S_R^2}{2}\right]^{\frac{1}{6}} \tag{53}$$

Cases were run using the following parameters: $R = 1m, U = 1m/s, v_0 = 4m^2/s$, yielding $Re = 0.25, We = \lambda_1$. A fixed ratio $\lambda_2/\lambda_1 = 1/9$ was used as in [16] and [46]. Weissenberg numbers were varied from 0.125 to 1.125 with increments of 0.125. This represented a *recoverable shear* range between 0.44 and 4, both inclusive.

In Fig. 18 results obtained with the proposed technique are presented and compared against the cited works. The yellow line represents the theoretical solution as obtained by Tanner [45]. It is possible to notice that the presented technique (blue line) yields results that very much agree with Tanner's theory for a wider We range. Even though the results for near Newtonian ranges present a higher error, the swelling ratios obtained are still in the same order and the increased range of applicability amounts to the merit of the approach here presented.

DOI: 10.1002/fld

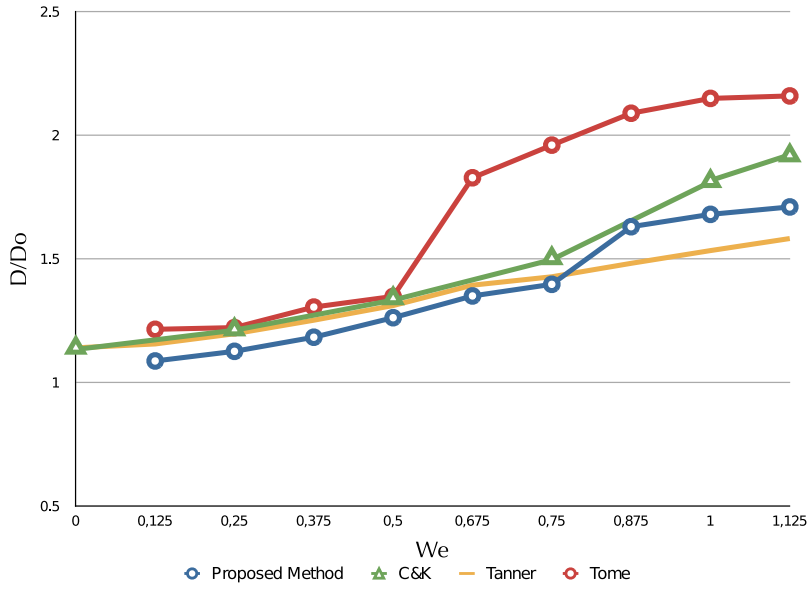

Figure 18. Swelling ratio against We. Different numerical models compared against an approximated theoretical solution by [45].

7.3. Drop Splashing. Worthington Jet

The third problem tackled was the simulation of a drop (both Newtonian and Oldroyd B fluids) impacting the free surface of a reservoir of the same fluid. At certain velocity this impact produces a crater around which a crown is usually formed. The crater is subsequently refilled and the filling fluid starts building up until a jet is formed. This splash was firstly studied by Worthington [49], who photographed low-viscosities Newtonian fluid splashes caused both by droplets and solid balls. Fig. 19 shows pictures taken at different stages of the experiment. In these it is possible to observe the crater, crown and satellite drops caused by the impact; and the jet formed shortly afterwards. In this case the resulting jet was discontinuous, forming a droplet.

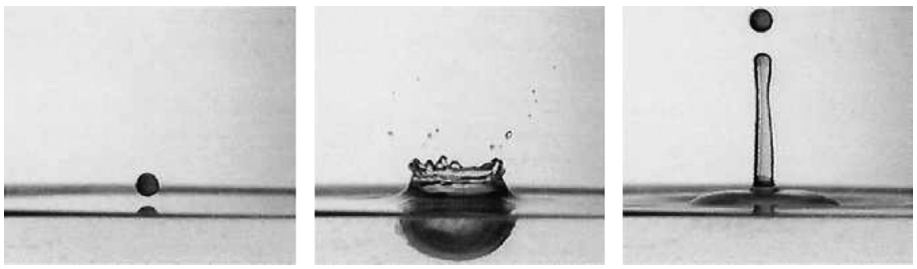

Figure 19. Drop falling, example of a Worthington Jet formation. (Taken from [14])

When studying the drop of a ball, Worthington was able to identify two kind of splashes, depending on whether the ball had a smooth surface or if it was rough. The drop of a small polished dry ball would slip in the fluid without almost any disturbance, this was denominated a “smooth splash”. On the other hand, “rough splashes” would appear when the ball was ground with a coarse sand paper or when it was left wet. In this case the sphere would produce the aforementioned crater and and jet. He also determined other factors which would govern the kind of splash formed. For

DOI: 10.1002/fld

instance, he showed that as the impact velocity increased a gradual transition from the smooth to rough splash occurred.

In the case of falling drops, Worthington classified the resulting splash as rough. However not all drops would produce a splash. Some drops simply produce vortex rings in the reservoir but nothing else. In this case the size of the droplet along with the impact velocity are the factor which determine the kind of behaviour that would take place.

In their work on the subject, [14] addressed the question on whether the surface tension influenced the splash by carrying on a series of experiments on Newtonian fluids with different surface tension but being equal all other parameters. They were able to conclude that the maximum jet height did not depend on the surface tension [14]. Another finding of this job was that a small increase in polymer concentration (thus augmenting the elasticity of the solution) reduced drastically the maximum jet height. It is precisely this behavior which constitutes the objective of this section. They also determined the necessary conditions to ensure that the splash experiment could be free of the influence of the reservoir walls [13].

The experiment setup included a drop of radius $r_d = 0.5$ cm falling on a circular tank of radius $r_t = 10$ cm and height $h_t = 10$ cm. As can be seen on [13], this tank dimension ensure that the non Newtonian drop will behave as if it were falling on an infinite reservoir. For the Newtonian case the reservoir might create some interference according to the data published, yet those experiments were performed with solid spheres of a diameter 50 percent larger than our drop. This give us confidence that this factor will not affect the results. Still the height of the jet should be very close to the maximum reachable even in the case of some wall interference.

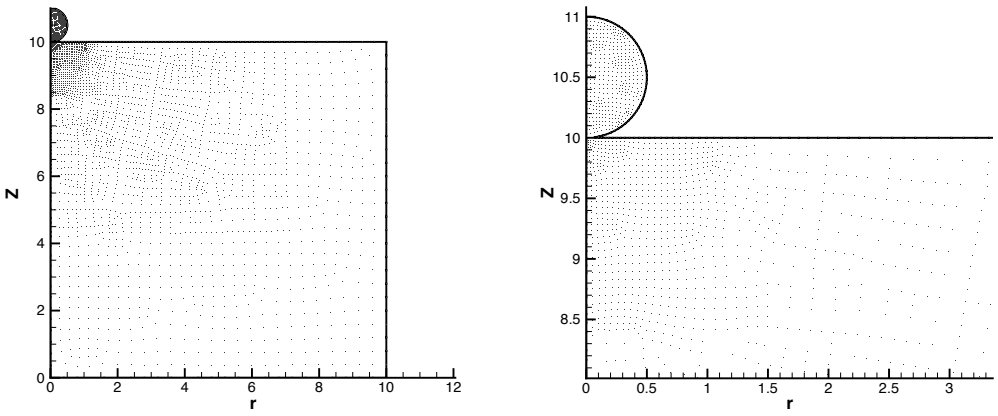

Figure 20. Initial configuration for the falling drop (left) and detail in the vicinity of the drop (right).

The initial configuration can be seen in Fig. 20. The simulation starts one step prior to the impact, at a time when the drop is travelling with a speed of $200cm/s$. The nodal density was increased in near the impact zone and inside de drop in order to have enough particles to properly describe the crown and jet.

We performed a series of simulations to be able to appreciate the viscoelastic effects due to an increase in the Weissenberg number. This was an attempt to simulate the different behaviour observed in [14] for fluids with the same viscosity i.e., flows at the same Reynolds number, but containing polymers of different stiffness. Following the steps of [46], a kinematic viscosity $\nu_0 = 0.2cm^2/s$ was considered which, after defining the Reynolds number as $Re = Ur_t/\nu_0$ would yield $Re = 500$. The cited work repeated the simulations at $Re = 1000$ and 2000 but showed that the only real difference at this ranges was that the jet heights were higher as Re increased.

Figure 21 shows the apex reached by each of the test fluids. In this case the non-Newtonian fluids had a We_{ef} of 0.1 and 0.5 respectively. As expected, the lower obtained jet heights corresponded to more non-Newtonian behaviours. Even though the obtained jets are lower than those observed in

DOI: 10.1002/fld

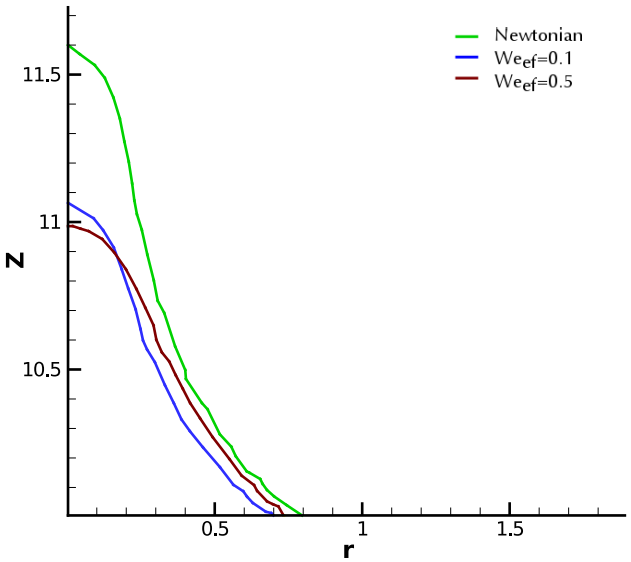

Figure 21. Maximum height reached by the Newtonian fluid and Oldroyd fluids of $We_{ef} = 0\ 1$ and $We_{ef} = 0\ 5$.

the laboratory, the results still agree qualitatively with the actual behaviour. Figures 22 and 27 show the evolution of the splash as well as allow us to contrast the process both for a Newtonian fluid and an Oldroyd B fluid.

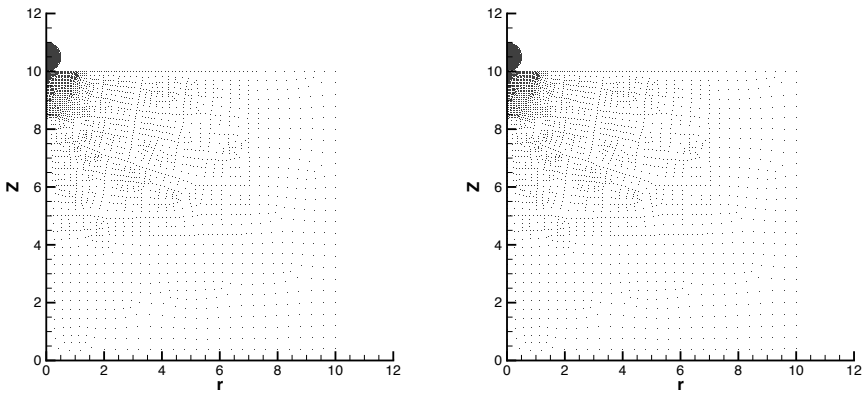

Figure 22. Comparision between Newtonian fluid (left) and Oldroyd B fluid (right) with $We = 0\ 5$. $t = 0$

8. CONCLUSIONS

The technique introduced in this work represents an efficient alternative to simulate free-surface non-Newtonian flows in situations where a traditional Eulerian or ALE approach would present

Prepared using fldauth.cls
DOI: 10.1002/fld

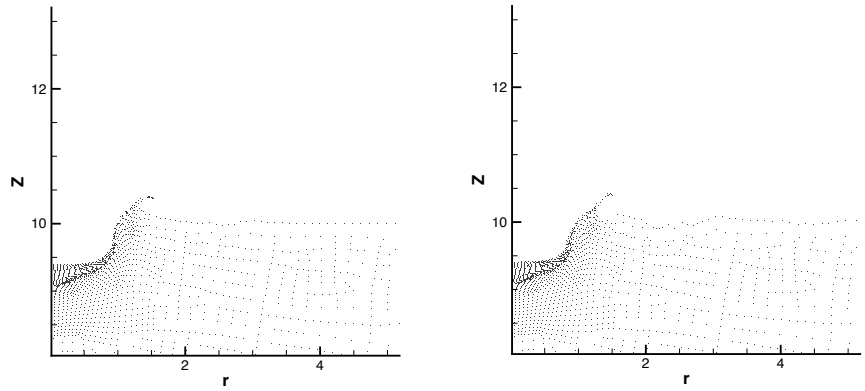

Figure 23. t=10 ms. The crown is visible at this point.

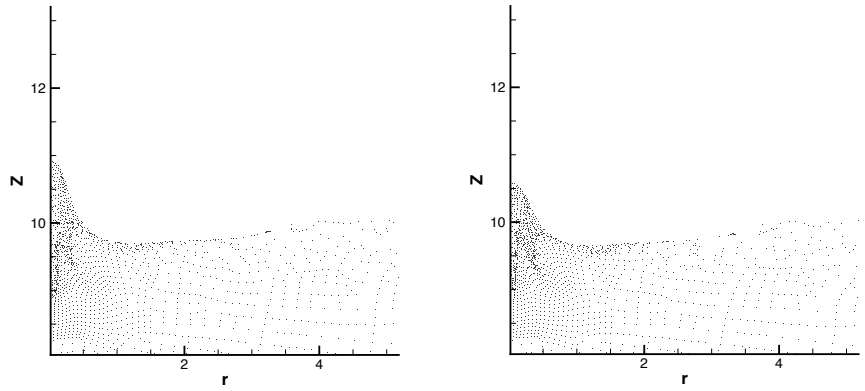

Figure 24. t=75 ms. The jet is already formed.

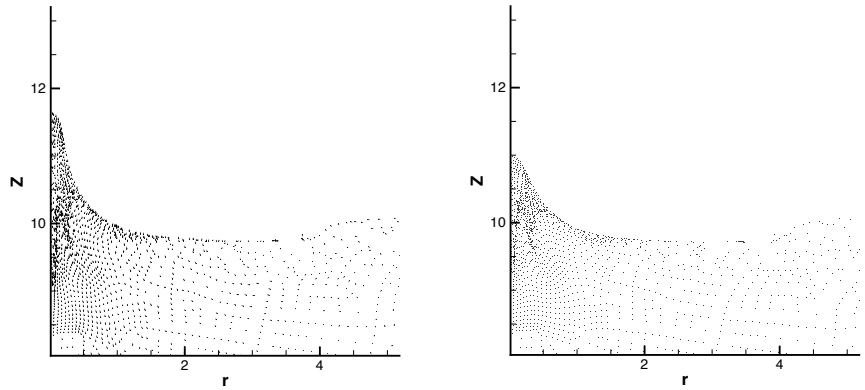

Figure 25. t=105 ms. Oldroyd fluid reaches its maximum height.

difficulties. Furthermore, since the method in built in an updated Lagrangian framework, it presents itself as an excellent option for keeping a nodal structure. The history of extra-stresses can thus

DOI: 10.1002/fld

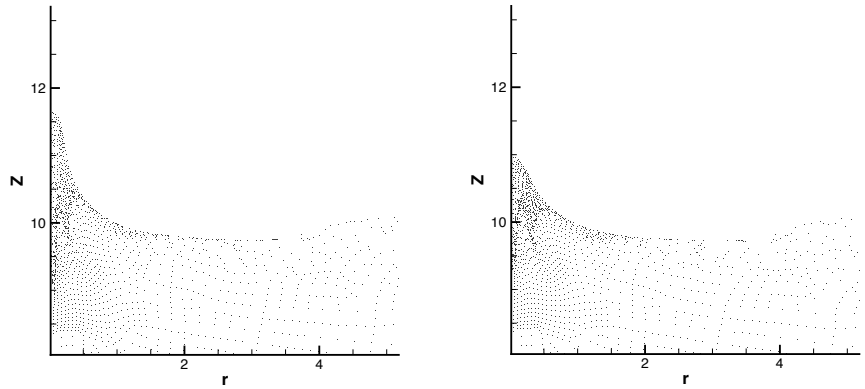

Figure 26. t=110 ms. Newtonian fluid reaches its maximum height.

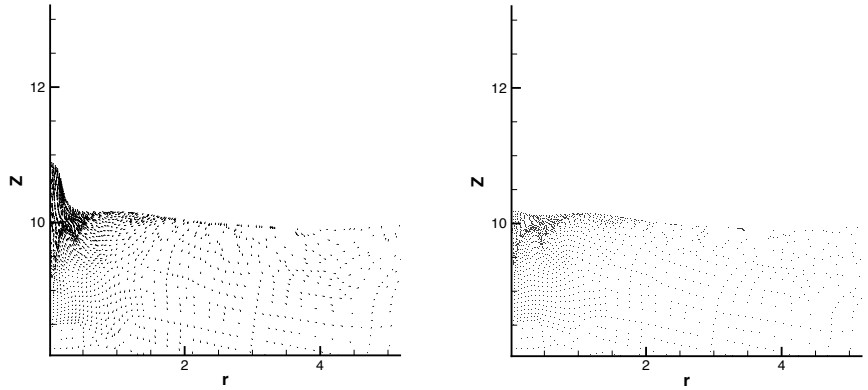

Figure 27. t=150 ms. Both jets are already decreasing.

be stored at nodal positions without the need to resource to interpolation techniques or the need to calculate in points other than the nodes. In fact this might be the most important facet of this experience. It has been shown that the NEM is totally able to successfully work with nodal properties in situations where the cloud configuration change is large.

The proposed method is able to reproduce with great accuracy analytical solutions where available. In addition, it works well for moderate We numbers, better than existing state-of-the-art techniques. This superior behaviour could probably be attributed to the excellent quality of natural neighbour interpolation in highly distorted meshes, a fact reported by various authors in the literature.

In any case, the distinct features of the method, namely an updated Lagrangian framework, the use of natural neighbour interpolation in a Galerkin setting, a second-order time discretisation algorithm for inertial terms, and a nodal implementation, together with state-of-the-art techniques for nodal cloud shape reconstruction on the fly, make this method an appealing choice for the simulation of Newtonian and, specially, non-Newtonian free-surface flows.

REFERENCES

1. I. Alfaro, J. Yvonnet, F. Chinesta, and E. Cueto. A study on the performance of Natural Neighbour-based Galerkin Methods. *International Journal for Numerical Methods in Engineering*, 71:1436?1465, 2007.

DOI: 10.1002/fld

2. Nina Amenta, Marsahll Bern, and Manolis Kamvysselis. A new voronoi-based surface reconstruction algorithm. In *Siggraph 98*, pages 415–421, 1998.
3. Nina Amenta, Marshall Bern, and David Eppstein. The crust and the beta-skeleton: combinatorial curve reconstruction. *Graphical Models and Image Processing*, 60/2:2:125–135, 1998.
4. M. Arroyo and M. Ortiz. Local maximum-entropy approximation schemes: a seamless bridge between finite elements and meshfree methods. *International Journal for Numerical Methods in Engineering*, 65(13):2167–2202, March 2006.
5. I. Babuška and A. Aziz. On the angle condition in the finite element method. *SIAM J. Numer. Anal.*, 13:214–227, 1976.
6. V. V. Belikov, V. D. Ivankov, V. K. Kontorovich, S. A. Korytnik, and A. Yu. Semenov. The non-Sibsonian interpolation: A new method of interpolation of the values of a function on arbitrary set of points. *Computational Mathematics and Mathematical Physics*, 37(1):9–15, 1997.
7. T. Belytschko, Y. Krongauz, D. Organ, M. Fleming, and P. Krysl. Meshless Methods: An Overview and Recent Developments. *Computer Methods in Applied Mechanics and Engineering*, 139:3–47, 1998.
8. T. Belytschko, Y. Y. Lu, and L. Gu. Element-Free Galerkin Methods. *International Journal for Numerical Methods in Engineering*, 37:229–256, 1994.
9. J. Birknes and G. Pedersen. A particle finite element method applied to long wave run-up. *International Journal For Numerical Methods In Fluids*, 52:237–261, 2006.
10. K. Boukir, Y. Maday, B. Métivet, and E. Razafindrakoto. A high-order characteristic/finite element method for the incompressible navier-stokes equations. *International Journal for Numerical Methods in Fluids*, 25:1421–1454, 1997.
11. F. Cazals, J Giesen, M Pauly, and A. Zomorodian. The conformal alpha-shape filtration. *The Visual Computer*, 22(8):531–540, 2006.
12. Jiun-Shyan Chen, Cheng-Tang Wu, Sangpil Yoon, and Yang You. A stabilized conforming nodal integration for Galerkin mesh-free methods. *International Journal for Numerical Methods in Engineering*, 50:435–466, 2001.
13. J. M. Cheny and K. Walters. Extravagant viscoelastic effects in the worthington jet experiment. *Journal of Non-Newtonian Fluid Mechanics*, 67:125 – 135, 1996. Papers Presented at the Workshop on 'Unresolved Experimental Dilemmas in the Dynamics of Complex Fluids'.
14. J. M. Cheny and K. Walters. Rheological influences on the splashing experiment. *Journal of Non-Newtonian Fluid Mechanics*, 86(1-2):185 – 210, 1999.
15. M.J. Crochet, A.R. Davies, and K. Walters. *Numerical Simulation of Non-Newtonian Flow*. Elsevier, 1984.
16. M.J. Crochet and R. Keunings. Finite element analysis of die swell of a highly elastic fluid. *Journal of Non-Newtonian Fluid Mechanics*, 10(3-4):339 – 356, 1982.
17. M.J. Crochet and K. Walters. Numerical methods ind non-newtonian fluid mechanics. *Anual Review of Fluid Mechanics*, 15:241–260, 1983.
18. E. Cueto, M. Doblaré, and L. Gracia. Imposing essential boundary conditions in the Natural Element Method by means of density-scaled α-shapes. *International Journal for Numerical Methods in Engineering*, 49-4:519–546, 2000.
19. E. Cueto, N. Sukumar, B. Calvo, M. A. Martínez, J. Cegoñino, and M. Doblaré. Overview and recent advances in Natural Neighbour Galerkin methods. *Archives of Computational Methods in Engineering*, 10(4):307–384, 2003.
20. B. Delaunay. Sur la Sphére Vide. A la memoire de Georges Voronoi. *Izvestia Akademii Nauk SSSR, Otdelenie Matematicheskii i Estestvennyka Nauk*, 7:793–800, 1934.
21. J. Donea. Arbitrary Lagrangian-Eulerian finite element methods. In T. Belytschko and T. J. R. Hughes, editors, *Computer methods for transient analyses*, pages 474–516. Elsevier-Amsterdam, 1983.
22. J. Donea and A. Huerta. *Finite Element Methods for Flow Problems*. John Wiley and sons, 2003.
23. L. Duchemin, S. Popinet, C. Josserand, and S. Zaleski. Jet formation in bubbles bursting at a free surface. *Physics of Fluids*, 14:3000–3008, 2002.
24. S Fernandez-Mendez and A Huerta. Imposing essential boundary conditions in mesh-free methods. *COMPUTER METHODS IN APPLIED MECHANICS AND ENGINEERING*, 193(12-14):1257–1275, 2004.
25. A. Galavis, D. González, I. Alfaro, and E. Cueto. Improved boundary tracking in meshless simulations of free-surface flows. *Computational Mechanics*, (42):467–479, 2008.
26. J. Giesen and M. John. The Flow Complex: A data structure for geometric modelling. In *Proceedings of the 14th Annual ACM-SIAM symposium on DiscreteAlgorithms*, pages 285–294, 2003.
27. D. González, E. Cueto, F. Chinesta, and M. Doblaré. A natural element updated Lagrangian strategy for free-surface fluid dynamics. *Journal of Computational Physics*, 223(1):127–150, 2007.
28. D. González, E. Cueto, and M. Doblaré. Volumetric locking in Natural Neighbour Galerkin methods. *International Journal for Numerical Methods in Engineering*, 61(4), 2004.
29. D. González, E. Cueto, and M. Doblaré. Higher-order natural element methods: Towards an isogeometric meshless method. *Int. J. Numer. Meth. Engng.*, 74(13):1928–1954, June 2008.
30. D. Gonzalez, E. Cueto, and M. Doblare. A higher order method based on local maximum entropy approximation. *International Journal for Numerical Methods in Engineering*, 83(6):741–764, 2010.
31. D. González, E. Cueto, M. A. Martinez, and M. Doblaré. Numerical integration in Natural Neighbour Galerkin methods. *International Journal for Numerical Methods in Engineering*, 60(12):2077–2104, 2004.
32. S. R. Idelsohn, E. Oñate, N. Calvo, and F. del Pin. The meshless finite element method. *International Journal for Numerical Methods in Engineering*, 58:893–912, 2003.
33. S. R. Idelsohn, E. Oñate, and F. del Pin. The particle finite element method: a powerful tool to solve incompressible flows with free-surfaces and breaking waves. *International Journal for Numerical Methods in Engineering*, 61 (7):964–989, 2004.
34. P. Lesaint and P.A. Raviart. On a finite element method for solving the neutron transport equation. *Mathematical Aspectst of Finite Elements in Partial Diferencial Equations*, pages 89–123, 1974.

DOI: 10.1002/fld

35. R. W. Lewis, S. E. Navti, and C. Taylor. A mixed lagrangian-eulerian approach to modelling fluid flow during mould filling. *International Journal for Numerical Methods in Fluids*, 25:931–952, 1997.
36. J.M. Marchal and M.J. Crochet. A new mixed finite element method for calculating viscoelastic flow. *Journal of Non-Newtonian Fluid Mechanics*, 20:187–207, 1987.
37. E. Oñate, S. Idelsohn, O. C. Zienkiewicz, R. L. Taylor, and C. Sacco. A stabilized finite point method for analysis of fluid mechanics problems. *Computer Methods in Applied Mechanics and Engineering*, 139:315–346, 1996.
38. R.G. Owens and T.N. Phillips. *Computational Rheology*. Imperial College PRess, 2002.
39. Andrea Prosperetti. Motion of two superposed viscous fluids. *Physics of Fluids*, 24(7):1217–1223, 1981.
40. B. Ramaswamy. Numerical Simulation of Unsteady Viscous Free Surface Flow. *Journal of Computational Physics*, 90:396–430, 1990.
41. R. Sibson. A Vector Identity for the Dirichlet Tessellation. *Mathematical Proceedings of the Cambridge Philosophical Society*, 87:151–155, 1980.
42. N. Sukumar. *The Natural Element Method in Solid Mechanics*. PhD thesis, Northwestern University, Evanston, Illinois, 1998.
43. N. Sukumar, B. Moran, and T. Belytschko. The Natural Element Method in Solid Mechanics. *International Journal for Numerical Methods in Engineering*, 43(5):839–887, 1998.
44. N. Sukumar, B. Moran, A. Yu Semenov, and V.V. Belikov. Natural Neighbor Galerkin Methods. *International Journal for Numerical Methods in Engineering*, 50(1):1–27, 2001.
45. Roger I. Tanner. A theory of die-swell revisited. *Journal of Non-Newtonian Fluid Mechanics*, 129(2):85 – 87, 2005.
46. M.F. Tome, L. Grossi, A. Castello, J.A. Cuminato, S. McKee, and K. Walters. Die-swell, splashing drop and a numerical technique for solving the oldroyd b model for axisymmetric free surface flows. *Journal of Non-Newtonian Fluid Mechanics*, (141):148–166, 2007.
47. G. M. Voronoi. Nouvelles Applications des Parametres Continus a la Theorie des Formes Quadratiques. Deuxieme Memoire: Recherches sur les parallelloedres Primitifs. *J. Reine Angew. Math.*, 134:198–287, 1908.
48. K. Walters and M. F. Webster. The distinctive CFD challenges of computational rheology. *International Journal for Numerical Methods in Fluids*, 43(5):577–596, 2003.
49. A. M. Worthington. On the forms assumed by drops of liquid falling on a horizontal plate. *Proc. R. Soc. London*, 25:261, 1877.

DOI: 10.1002/fld